JGR Space Physics

RESEARCH ARTICLE
10.1029/2019JA027369

Examining Local Time Variations in the Gains and Losses of Open Magnetic Flux During Substorms

M. K. Mooney[1,2], C. Forsyth[1], I. J. Rae[1], G. Chisham[3], J. C. Coxon[4], M. S. Marsh[2], D. R. Jackson[2], S. Bingham[2], and B. Hubert[5]

[1]Mullard Space Science Laboratory, University College London, Dorking, UK, [2]Met Office, Exeter, UK, [3]British Antarctic Survey, Cambridge, UK, [4]Department of Physics and Astronomy, University of Southampton, Southampton, UK, [5]Laboratory for Planetary and Atmospheric Physics, Liege, Belgium

Key Points:
- We perform a statistical analysis of open flux content in the nightside ionosphere during substorms
- At substorm onset, the open flux decreases overall and in the substorm onset sector but increases in the dusk and dawn sectors
- The estimated rate of closure of the total nightside open flux content differs by up to 66% between the three IMAGE FUV instruments

Supporting Information:
- Supporting Information S1

Correspondence to:
M. K. Mooney,
m.mooney.16@ucl.ac.uk

Citation:
Mooney, M. K., Forsyth, C., Rae, I. J., Chisham, G., Coxon, J. C., Marsh, M. S., et al. (2020). Examining local time variations in the gains and losses of open magnetic flux during substorms. *Journal of Geophysical Research: Space Physics*, *125*, e2019JA027369. https://doi.org/10.1029/2019JA027369

Received 7 MAR 2019
Accepted 25 FEB 2020
Accepted article online 28 FEB 2020

Abstract The open magnetic flux content of the magnetosphere varies during substorms as a result of dayside and nightside reconnection. The open flux can be calculated from the area of the polar cap, delineated by the open-closed field line boundary (OCB). This study presents a superposed epoch analysis of the location of the OCB and the change in the magnetic flux content in individual nightside MLT sectors during substorm growth, expansion, and recovery phases. Far ultraviolet (FUV) observations from the IMAGE satellite are used to derive a proxy of the OCB location. In the hour prior to substorm onset, the total nightside flux content increases by up to 0.12 GWb on average, resulting in an equatorward expansion of the OCB. Following substorm onset, the OCB contracts toward the pole as the open magnetic flux content decreases by up to 0.14 GWb on average, but the rate of decrease of the total nightside open flux content differs by 5–66% between the three IMAGE far ultraviolet instruments. The OCB does not contract poleward uniformly in all nightside magnetic local time (MLT) sectors after substorm onset. Close to the substorm onset MLT sector, the OCB contracts immediately following substorm onset; however, the OCB in more dawnward and duskward MLT sectors continues to expand equatorward for up to 120 minutes after substorm onset. Despite the continued increase in flux in these sectors after substorm onset, the total nightside flux content decreases immediately at substorm onset, indicating that the nightside reconnection rate exceeds the dayside rate following substorm onset.

Plain Language Summary Earth's magnetic field shields us from the steady stream of particles originating from the Sun, which carry the Sun's magnetic field. At Earth, the solar magnetic field can break open our magnetic field and allow energy to build up inside Earth's magnetic field. This energy can be explosively released during substorms. The auroral oval is a ring of aurora around the magnetic poles which varies in size, shape, and brightness during substorms. As energy is building in the magnetic field, the auroral oval expands. As the energy is released, it contracts. Using satellite images of the auroral oval, we show that prior to substorm onset, the nightside auroral oval expands toward the equator. At substorm onset, the auroral oval also rapidly moves poleward. The poleward motion initially occurs in a localized region as the rest of the nightside oval continues to expand. The poleward motion then spreads eastward and westward around the entire nightside oval over the following 20–120 minutes. Our results show that although most of the auroral oval continues to expand equatorward after substorm onset, the total area of the auroral oval decreases resulting in an overall net decrease in the energy stored in the Earth's magnetic field.

1. Introduction

The Dungey (1961) Cycle describes the interaction between the Earth's magnetosphere and the interplanetary magnetic field (IMF) frozen into the solar wind. In a simplified case where the IMF has a strongly southward orientation, magnetic reconnection at the dayside magnetopause leads to the opening of closed magnetic field lines of Earth's magnetosphere. The foot points of the open magnetic field lines are in the polar cap, the region encircled by the auroral oval. The open magnetic field lines convect through the lobes to the nightside magnetosphere, and their footpoints cross the polar cap. Magnetic reconnection in the magnetotail acts to close open magnetic field lines. The newly closed magnetic field lines convect sunward, restoring the structure of the dayside magnetosphere. The open flux content of the polar caps, F_{PC}, varies

due to the relative rates of dayside and nightside reconnection (Cowley & Lockwood, 1992; Milan et al., 2007; Siscoe & Huang, 1985; Walach et al., 2017):

$$\frac{dF_{PC}(t)}{dt} = \Phi_D(t) - \Phi_N(t), \quad (1)$$

where Φ_D and Φ_N are the rates of dayside and nightside reconnection, respectively, calculated from the electrostatic potential integrated over the X-line reconnection region.

The edge of the polar cap is defined as the open-closed field line boundary (OCB), and the area of the polar cap indicates the open flux content of the magnetosphere. The location of the OCB is closely associated with, although not directly equivalent to, the poleward edge of the auroral oval (Baker et al., 2000; Hubert et al., 2006; Kauristie et al., 1999; Rae et al., 2004). By comparing auroral observations and in situ observations of the precipitating particles, local-time dependent corrections to the auroral boundary can be determined to provide the location of the OCB from auroral measurements (Boakes et al., 2008; Carbary et al., 2003; Longden et al., 2010). As the open flux content of the magnetosphere increases in response to dayside reconnection with southward oriented IMF, magnetic flux is distributed around the polar cap by excited plasma flows (Cowley & Lockwood, 1992), and the auroral oval and OCB expand toward the equator. Similarly, a decrease in the open flux content from enhanced magnetotail reconnection leads to a reduction in the polar cap area, and the OCB contracts toward the pole. The changing size of the polar cap in response to reconnection is known as the expanding and contracting polar cap (ECPC) paradigm, proposed by Cowley and Lockwood (1992).

Substorms are a dynamic magnetospheric process which result in rapid changes in open magnetic flux; thus, the ECPC paradigm is a key concept in their understanding. Substorms have three distinct phases: growth, expansion, and recovery (Akasofu, 1964; McPherron, 1970), and have a duration on the order of 3 hours on average (Tanskanen, 2009). The substorm growth phase has an average duration of 40 minutes to over an hour (Coumans et al., 2007). The substorm expansion phase period is typically 20–30 minutes (Chu et al., 2015 ; Forsyth et al., 2015; Gjerloev et al., 2007), and the recovery phase lasts 30–40 minutes on average, as determined from ground magnetometer data (Chu et al., 2015; Forsyth et al., 2015).

During the growth phase, it is generally considered that the rate of dayside reconnection dominates over the rate of nightside reconnection. As a consequence, the open magnetic flux accumulates in the magnetosphere, which results in an increase in the polar cap area and an equatorward motion of the OCBs (Boakes et al., 2011; Milan et al., 2008). During the expansion and recovery phases, nightside reconnection generally becomes dominant, closing open flux and causing the polar cap area to shrink. However, as shown by equation 1, the change in the polar cap is determined by the relative rates of reconnection at the dayside and nightside; thus, open flux may continue to accumulate in the magnetosphere during the substorm expansion and recovery phases if dayside reconnection is ongoing at a faster rate than nightside reconnection (Clausen et al., 2013; Coumans et al., 2007; Coxon et al., 2014; Kallio et al., 2000; Milan, Hutchinson, et al., 2009).

The beginning of the substorm expansion phase is termed “substorm onset” and can be identified by a sudden brightening in one of the equatorward arcs in nightside auroral oval (Akasofu, 1964). Early observations of auroral substorms made by Akasofu (1964) observed the bright onset auroral arc moving poleward rapidly after substorm onset, forming the auroral bulge in the substorm onset location. The auroral bulge expands westward, forming the westward traveling surge, eastward and poleward following substorm onset (Gjerloev et al., 2007). The westward and eastward expansions are initially fast at substorm onset but decrease during the substorm expansion phase (Gjerloev et al., 2007). The westward expansion of the auroral bulge has been observed to initially advance with a speed of 8 km/s (Craven et al., 1989) and gradually slows to 1 km/s as it expands (Craven et al., 1989). During the recovery phase, although the open flux content is expected to continue to decrease to a quiescent level, the morphology of the auroral oval can change from that observed in the expansion phase, with the morning sector aurora brightening during the recovery phase, while the evening sector aurora continues to decay (Opgenoorth et al., 1994).

Auroral substorms have been observed by satellites in polar orbits with distant apogees, allowing them to spend prolonged periods of time imaging the polar cap regions and auroral emission in both visible and ultraviolet (UV) wavebands, for example, Polar and IMAGE. UV images of the auroral oval obtained by IMAGE

have been used by Frey et al. (2004) and Frey and Mende (2007) to compile a list of substorm onsets, identified by the brightening of the nightside auroral oval which has led to both case and statistical studies of substorms (e.g., Coumans et al., 2007; Milan, Grocott, et al., 2009; Milan, Hutchinson, et al., 2009; Milan et al., 2010; Walach et al., 2017). Satellite observations have also been used in conjunction with radar data, such as SuperDARN and EISCAT, to infer the rates of dayside and nightside reconnection (Chisham et al., 2008; Hubert et al., 2006, 2010, 2017). In addition, many studies have used the poleward edge of the auroral oval from UV images as a proxy for the OCB location to estimate the open flux content of the polar caps (Boakes et al., 2008, 2009; Coumans et al., 2007; Hubert et al., 2006; Longden et al., 2010; Milan, Grocott, et al., 2009, Milan, Hutchinson, et al., 2009).

A superposed epoch analysis of UV auroral intensity during substorms by Milan, Hutchinson, et al. (2009) found that the latitude of the maximum intensity continues to move equatorward after substorm onset, particularly in the dawn and dusk regions of the auroral oval, while in the midnight sector, the location of the maximum intensity moves toward the pole immediately at substorm onset. Given that the auroral oval is linked to the polar cap, these results suggest that the movement of the OCB varies with local time. Clausen et al. (2012) showed that the location of the Region 1 (R1) Birkeland current system could also be used as a proxy for the OCB. By calculating the area of a circle fitted to the latitude of the R1 current in each local time sector, Clausen et al. (2013) and Coxon et al. (2014) presented two superposed epoch analyses of substorms using the R1 OCB proxy location to observe changes in the open magnetic flux content of the northern hemisphere polar cap during substorms. The results from these studies indicated that the open flux content continues to increase for up to 15–20 minutes after substorm onset, particularly in the dusk sector (Clausen et al., 2013). Clausen et al. (2013) and Coxon et al. (2014) suggested that the results were indicative of dayside reconnection continuing to dominate over nightside reconnection in the first 15–20 minutes after substorm onset in certain sectors. Similarly, a statistical analysis of 55 substorms by Coumans et al. (2007) found that on average, the open flux content remained constant or continued to increase within the first 20 minutes of substorm onset.

The findings presented in these studies are somewhat unexpected in the context of the standard substorm model that describes nightside reconnection immediately dominating over dayside reconnection at substorm onset to reduce the open flux content of the polar cap and thus causing the OCB to contract poleward immediately at substorm onset. The present study aims to look more closely at the expansion and contraction of the OCB in individual nightside magnetic local time (MLT) sectors, as well as the global motion of the nightside OCB, during the substorm growth and expansion phases in order to reconcile the recent findings with the substorm model. In this work, a superposed epoch analysis was performed on the OCB locations calculated from the poleward auroral boundary by Longden et al. (2010) during substorm periods identified by Frey et al. (2004). Section 2 provides a brief overview of the calculation of the OCB locations derived from IMAGE far UV (FUV) data and the superposed epoch analysis; section 3 presents the results obtained for mid-sized substorms occurring with onset latitudes between 64 – 66°; and section 4 discusses the main findings of the study.

2. Data and Method

2.1. IMAGE Data

The IMAGE satellite, in operation between 2000 and 2005, was in a precessing polar orbit with a perigee of 1,000 km and an apogee of 44,000 km (~7 Earth radii) (Mende, Heetderks, Frey, Lampton, Geller, Abiad, et al., 2000). Over the first 2 years of nominal operations between 2000 and 2002, the orbital apogee was situated over the northern hemisphere. During this period, the satellite was in an optimal position to capture images of the northern polar cap and auroral oval. The satellite captured FUV images of the Earth with three onboard cameras. The wideband imaging camera (WIC) was sensitive to emission in the 140–190 nm wavelength range dominated by the N2-Lyman-Birge-Hopfield band system (Mende, Heetderks, Frey, Lampton, Geller, Habraken, et al., 2000) while two narrower passband spectral imaging cameras, SI12 and SI13, centered on 121.8 and 135.6 nm, respectively (Mende, Heetderks, Frey, Stock, et al., 2000). The SI12 passband detected the Doppler-shifted Lyman-α emission due to the proton aurora while rejecting the geocoronal Lyman-α and the nearby intense emission of Nitrogen at 120 nm. The SI13 camera was sensitive

to 135.6 nm oxygen emission, mostly associated with electron precipitation (Mende, Heetderks, Frey, Stock, et al., 2000). Observation images were taken by each FUV instrument approximately every 2 minutes actuated by the spin period of the IMAGE satellite (Burch, 2000).

2.2. OCB Location Identification From IMAGE FUV Data

The poleward auroral boundary has long been taken as a proxy for the OCB. For a small number of events, Milan et al. (2003) found excellent correspondence between the location of the poleward auroral boundary from individual FUV observations and the OCB location determined from DMSP particle precipitation measurements. The location of the auroral boundary relative to particle precipitation boundaries, which are taken to be the "true" open-closed field-line boundary, has been calculated, and thus, global auroral images can be used to calculate the amount of open flux in the magnetosphere (Boakes et al., 2008; Carbary et al., 2003; Longden et al., 2010). Longden et al. (2010) determined the location of the poleward auroral luminosity boundary (PALB) from the IMAGE FUV data and then determined the statistical offset between this boundary and the OCB location determined from particle precipitation measurements from DMSP to provide a correction factor from which the OCB location can be calculated. Poleward boundaries were derived for each of the three FUV instruments onboard IMAGE by dividing images of the northern polar cap into 24 MLT sectors and creating a latitudinal intensity profile of the UV emission for each sector. Each intensity profile was fitted with two model functions: a single Gaussian modeling a continuous auroral oval with no bifurcation or splitting or a double Gaussian which better models a bifurcated auroral oval. The goodness of fit of the two model functions was evaluated in each MLT sector using the reduced χ^2 statistic. If the single Gaussian model function provides a better fit, the PALB is identified as the poleward full width half maximum of the Gaussian peak. If the double Gaussian model function is a better fit, the PALB is identified to be at the poleward full width half maximum of the most poleward Gaussian peak. The method follows a similar approach to the techniques of Carbary et al. (2003) and Boakes et al. (2008), which both fitted single Gaussian functions to the luminosity profiles, and the method of Mende et al. (2003), which used a double Gaussian profile to account for bifurcation or splitting of the auroral oval. Fitting both Gaussian functions allows for automation without prior knowledge of the level of bifurcation, or splitting, in the auroral oval in different MLT sectors (Longden et al., 2010).

Statistical studies have shown that the true location of the OCB determined from precipitating particle fluxes measured by low-Earth orbiting spacecraft can be offset from the auroral boundary by several degrees (Boakes et al., 2008; Carbary et al., 2003; Kauristie et al., 1999). These precipitating particle fluxes are usually only available four times per spacecraft orbit and provide a local determination of the OCB location. In contrast, auroral imagers such as the FUV cameras provide a global snapshot of the location of the aurora, thus the poleward boundary of the UV oval provides a useful global proxy for the OCB. Boakes et al. (2008) characterized the difference between the DMSP particle precipitation data and the UV poleward auroral oval boundary for each of the IMAGE FUV instrument data sets (WIC, SI12, and SI13) in each MLT sector. Longden et al. (2010) extended the work of Boakes et al. (2008) to determine the correction factors in each MLT and for each of the FUV cameras for their poleward auroral boundaries. Similarly to Boakes et al. (2008), Longden et al. (2010) found that for all FUV data sets, the PALBs near noon and midnight were found to lie poleward of the OCB location determined from DMSP particle precipitation measurements. In the dawn sectors, SI12 PALBs were also found to lie poleward of the particle precipitation OCB, while the WIC and SI13 PALBs required little correction in this region. In the dusk sectors, the SI12 PALBs were located slightly equatorward, while the SI13 and WIC PALBs were poleward of the OCB location determined from DMSP particle precipitation measurements. We direct the interested reader to the full description of the method and example figures illustrating the proxy OCB location compared to the auroral FUV emission published in Longden et al. (2010). In the present study, we use the proxy OCB locations from Longden et al. (2010) with the average corrections applied in our superposed epoch analysis.

The Longden et al. (2010) method is most successful in locating the OCB in nightside MLT sectors compared to the dayside MLT sectors, possibly due to dayglow effects or because the dayside auroral oval is thinner and dimmer than the nightside. As such, we limit our analysis to the nightside MLT sectors. This is discussed further in section 3.1.

2.3. Superposed Epoch Analysis

Milan, Grocott, et al. (2009) performed a superposed epoch analysis of substorm auroral brightness for a list of substorms identified in the IMAGE FUV data by Frey et al. (2004). In that study, Milan, Grocott, et al. (2009) subdivided the substorms into five categories based on their onset latitude, Λ_{onset}:

1. $\Lambda_{onset} < 62°$.
2. $62° \geq \Lambda_{onset} < 64°$.
3. $64° \geq \Lambda_{onset} < 66°$.
4. $66° \geq \Lambda_{onset} < 68°$.
5. $\Lambda_{onset} \geq 68°$.

Using these onset latitude categories, Milan, Grocott, et al. (2009) found that lower onset latitude substorms resulted in larger expansions of the auroral oval in the midnight MLT sector. In order to ensure our statistical results are not unduly influenced by these larger events and to aid comparisons with other studies, we similarly subdivide our analysis by substorm onset latitude. Milan, Grocott, et al. (2009) showed the distribution of substorm onset MLT and onset latitude from substorms identified in the Frey et al. (2004) list between May 2000 and April 2002. The analysis performed by Milan, Grocott, et al. (2009) indicated that the majority of substorm onsets occurred in the premidnight MLT sectors between MLT 21 and MLT 00 and had onset latitudes between 66° and 68°. We find no significant difference in the substorm onset MLT distributions in each substorm onset latitude category.

We carried out a superposed epoch analysis of the OCB latitude from WIC, SI12, and SI13 keyed to substorm onset covering the hour prior to substorm onset and 2 hours after substorm onset. Given that substorm onset does not always occur in the same MLT sector, variations in the OCB are examined in MLT sectors relative to the onset MLT, effectively rotating each OCB so that the substorm onset MLTs were colocated (e.g., Coxon et al., 2017; Provan et al., 2004). As we are particularly interested in the poleward contraction of the OCB after substorm onset in each MLT sector, this rotation acts to minimize the spreading of the results of the superposed epoch analysis over a range of MLT sectors.

Due to the spin of the spacecraft, there is an interval of just over 2 minutes between the images collected by the IMAGE FUV instruments and hence between the OCB identifications. Prior to the superposed epoch analysis, we linearly interpolated the time series of OCB latitudes in each MLT to a regular 2 minute cadence. In the superposed epoch analysis, we do not require the proxy OCB location to be identified in all MLT sectors at all times.

Our analysis showed distinctly different results for the highest latitude substorms (greater than 68°). Further investigation of these showed that Longden et al. (2010) technique was occasionally fitting the PALB to bright, low-latitude artifacts in the FUV data, particularly data from the SI12 camera, prior to substorm onset when the auroral oval was dimmer. This effect was limited to the high-latitude category; hence, we present results for substorms with onsets latitudes up to 68° only.

3. Results

In the following, we show the results of the superposed epoch analysis of the OCB location for substorms with onset latitudes between 64° and 66°. This group of substorms contains 581 substorms and is in the middle of the substorm onset latitude categories in this study and as such contains the "midsized" substorms. Morphologically, the results of this substorm onset latitude category are generally representative of the other substorm onset latitude categories.

The superposed epoch analysis of the OCB location was performed on each data set obtained from the three FUV instruments onboard IMAGE (WIC, SI12, and SI13). We present the results of each instrument separately for comparison. For completeness, similar figures to those shown in Figures 1 and 2 for all substorm onset latitude categories are presented in the supporting information. Figures similar to those shown in Figures 3 and 5 using the SI12 and SI13 data sets are also presented in the supporting information.

3.1. Successful Boundary Identifications in Each MLT Sector

In the list of substorm onsets identified by Frey et al. (2004), 581 substorms were observed to brighten at a latitude between 64° and 66°. If there was a data gap of 10 minutes or more in the hour before or 2 hours

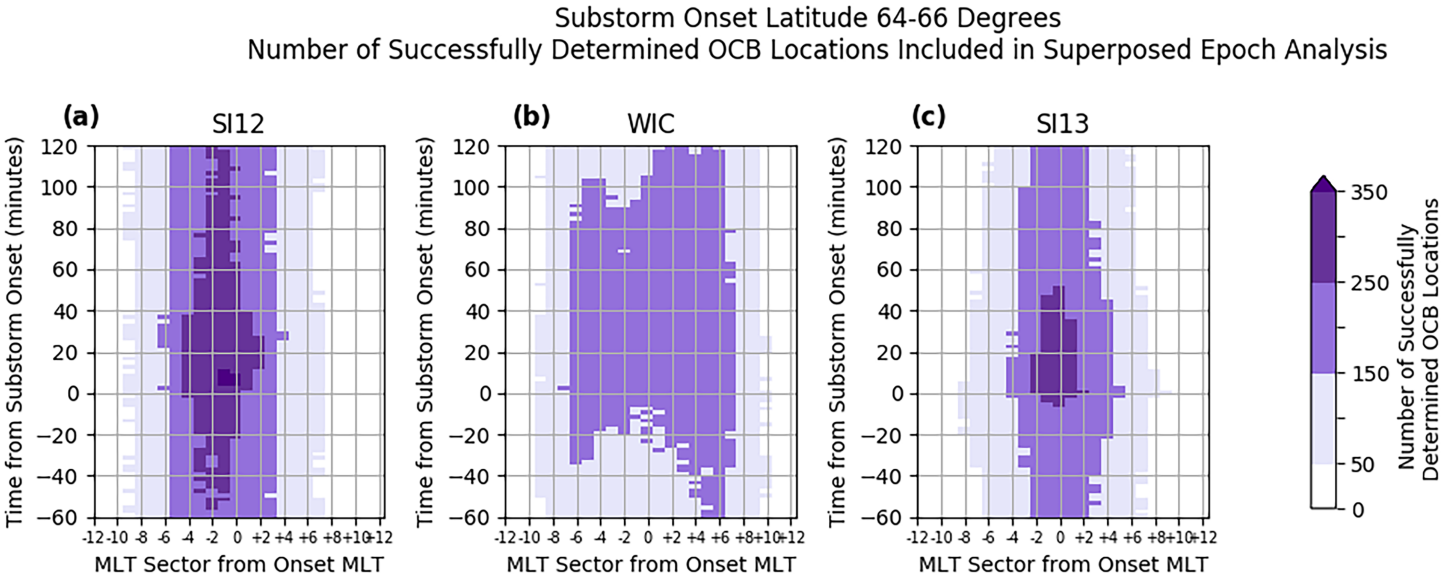

Figure 1. Plots showing the number of successfully fitted OCB locations in each MLT sector at each time step during the 3 hours superposed epoch analysis. The color bar shows five discrete levels to highlight times and MLT sectors which contain a particularly high or low number of successful OCB identifications. The steps with less than 50 data points, indicated in white, have been excluded from the analysis. Panels (a)–(c) show the number of successfully determined OCB locations from SI12, WIC, and SI13 data, respectively.

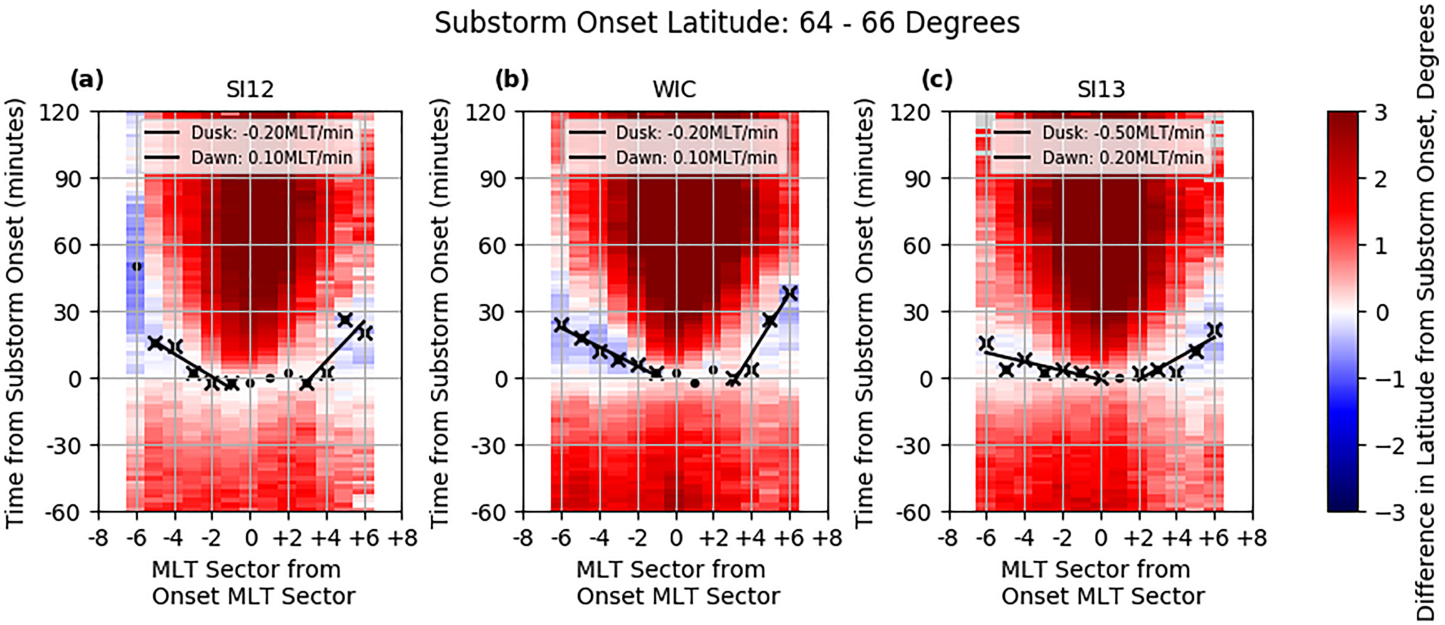

Figure 2. The results of the superposed epoch analysis of the OCB location from SI12, WIC, and SI13 ((a)–(c) respectively). The panels show the difference between the OCB location in each MLT sector with its location at substorm onset and with respect to time for substorms with onset latitudes between 64° and 66°. Red indicates that the OCB is located poleward of its location at onset; blue indicates the OCB is located equatorward of its location at onset. Gray indicates when there were less than 50 successfully identified OCB locations. The black dots and crosses indicate the time at which the OCB reaches its most equatorward location in each MLT sector. Two lines of best fit are calculated using the dawnward and duskward data points marked with crosses. The slopes of these two lines are displayed in the legend in each panel. The slopes of the lines of best fit for all substorm onset latitudes are provided in Table 1.

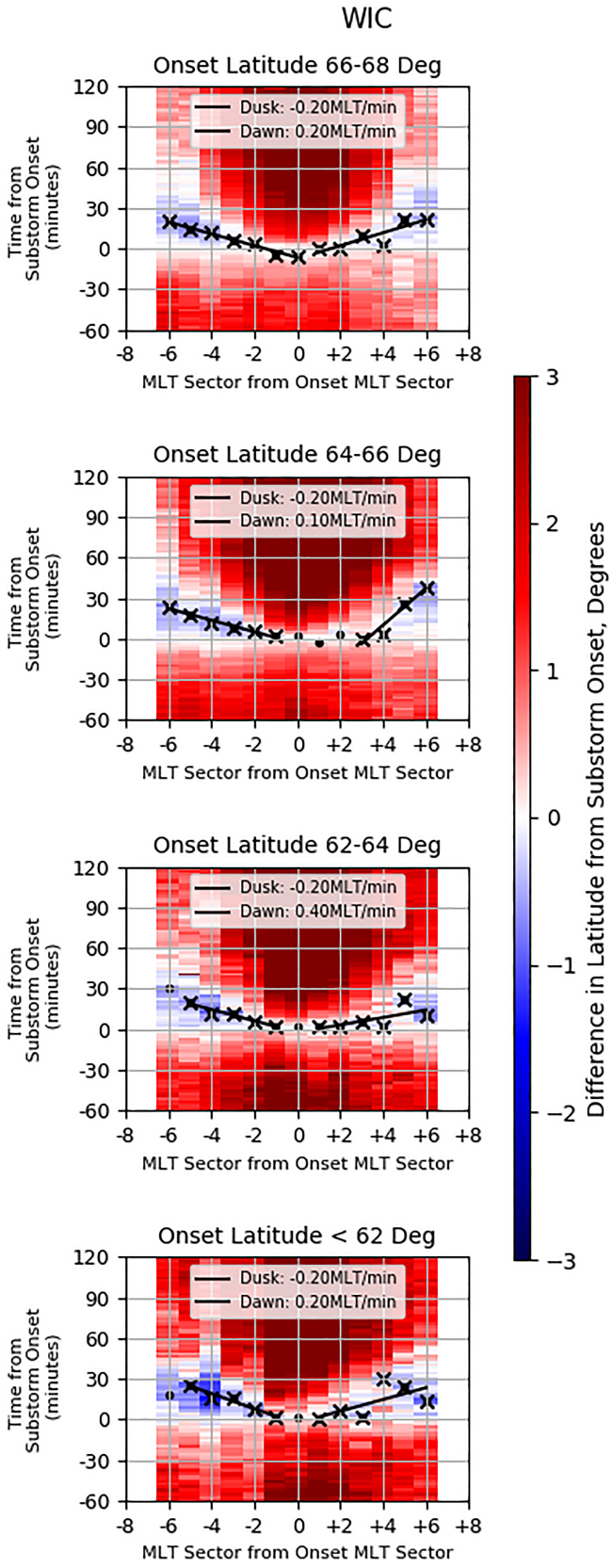

Figure 3. The results of the superposed epoch analysis using WIC data for substorms with onset latitudes in the ranges (a) 66–68°, (b) 64–66°, (c) 62–64°, and (d) <62°, presented as per Figure 2.

following onset, the event was not included in the superposed epoch analysis. In the superposed epoch analysis, 451 substorms were included in the SI13 data, 469 in the WIC data, and 449 in the SI12 data. The OCB location did not have to be identified in all MLT sectors to be included in the analysis.

Figure 1 shows the number of successful OCB identifications in each MLT sector for the hour before and 2 hours following substorm onset for substorms with onset latitudes between 64° and 66°. The results are shown for each of the three FUV instruments, SI12 in Figure 1a, WIC in Figure 1b, and SI13 in Figure 1c. In Figures 1–3, the substorm onset MLT sector is defined to be MLT = 0, negative MLT sectors are duskward of the substorm onset MLT sector, and positive MLT sectors are dawnward of the substorm onset sector. On the y axis, time is defined from substorm onset at $t = 0$.

Figure 1 shows that successful boundary identifications varied with imager and with time. The highest number of successful boundary identifications in the WIC data at any 2 minute time interval is around 180, compared to more than 300 and 350 for SI13 and SI12, respectively. The numbers of the successful identifications in the WIC and SI13 data were relatively symmetric about the onset MLT, with at least 50 identifications in each MLT sector between −8 and +8 for WIC and between −6 and +6 for SI13. In contrast, there were more boundary identifications duskward of the onset sector for SI12, with at least 50 identifications in each MLT sector between −8 and +6. Despite the lower overall numbers of successfully fitted OCB locations from the WIC data compared to the SI12 and SI13 data, the number of successfully fitted OCB identifications in the WIC data is higher across a wider range of MLT sectors than in the spectral imaging data, particularly in the dawnward sectors. SI12 and SI13 both show higher numbers of boundary identifications in the onset sector and close to the onset time, with at least 250 identifications within −10 to +50 minutes of onset.

The higher number of successfully fitted boundaries for the spectral imaging cameras around substorm onset coincides with the rapid brightening of the auroral oval around the onset MLT sector at substorm onset and into the expansion phase. When the auroral oval is brighter compared to the background emission, the poleward edge of the auroral oval and hence the OCB location may be more easily identified by the technique derived by Longden et al. (2010). The higher number of successfully fitted boundaries near the substorm onset MLT sector prior to substorm onset may indicate preexisting auroral emission in the onset sector, as previously observed by Milan et al. (2010).

The successful identification of the OCB in each MLT sector varies for each FUV instrument. In all instruments, the boundaries are more successfully fitted in the nightside MLT sectors between MLT −6 and MLT +6 with far fewer (less than 50) fitted in the dayside MLT sectors. One reason for this is that the auroral emission in dayside MLT sectors is generally dimmer than that of the nightside MLT sectors, especially following substorm onset, making it more difficult to fit Gaussian functions to the latitudinal intensity profiles of the dayside sectors. Furthermore, models generally show the auroral oval to be thinner on the dayside (e.g., Carbary, 2005; Holzworth & Meng, 1975), which may make a Gaussian fit more challenging. Given the low number of fits on the dayside, we focus our analysis on the nightside MLT sectors between MLT −6 and MLT +6.

3.2. Superposed Epoch Analysis of the OCB Location in Nightside MLT Sectors During Substorms

Figure 2 shows the results of the superposed epoch analysis of the OCB location in the nightside MLT sectors over a 3 hours period covering 1 hours prior to substorm onset and 2 hours after substorm onset. Substorm onset is defined at $t = 0$. The panels in Figure 2 show the results from (a) SI12, (b) WIC, and (c) SI13. The panels in Figure 2 have been limited to show only the MLT sectors which contain 50 or more successfully fitted boundary identifications in each time step, as previously discussed in section 3.1. Gray time steps indicate where there are less than 50 successful boundary identifications. In each MLT sector, the latitude of the OCB in that sector at substorm onset has been subtracted from each time step to obtain the difference in the boundary location compared to at onset. Blue indicates the boundary was located at a lower latitude (equatorward) with respect to the latitude at substorm onset, and red indicates that the boundary was at a higher latitude (poleward) than at substorm onset. White indicates that there was almost no change in the latitude of the boundary compared to substorm onset. The black dots and crosses in Figure 2 indicate the time at which the OCB reaches its most equatorward location in each MLT sector, that is, the time after which the OCB contracted poleward. This will be discussed in more detail in section 3.3.

The results from all three instruments show that the OCB was located poleward of its location at substorm onset prior to substorm onset, as shown by the red shading in each cell. This shows that polar

cap was expanding and the OCB moved equatorward in all nightside MLT sectors in the hour prior to substorm onset, as expected to occur due to the accumulation of open flux during the substorm growth phase. At substorm onset, the OCB in the MLT sectors around the onset sector immediately began to contract poleward as shown by the change in color from white to red. In the WIC data, rapid poleward contraction of the OCB following onset occurs most quickly in the substorm onset sector, while the SI12 boundaries show a shift in the most rapid contraction toward dusk and the SI13 boundaries show a shift in the most rapid contraction toward dawn. The immediate poleward contraction of the OCB at substorm onset near the substorm onset MLT sector is indicative of open flux leaving these sectors, most likely due to the closure of flux around the onset MLT sector following substorm onset.

The MLT sectors further from the onset sector, both duskward and dawnward, show an extended period of continued equatorward motion of the OCB after substorm onset. This continued equatorward motion is indicated by the extended white and blue regions of the figure after $t = 0$. The OCBs determined from all three imagers continued to expand equatorward for up to around 20 minutes after substorm onset in MLT −6 sector and for 20–40 minutes after substorm onset in the MLT +6 sector. The OCBs in the more duskward and dawnward sectors remained equatorward of their location at onset for some time but contracted poleward within an hour of substorm onset.

3.3. Rate of the Apparent Motion of the OCB Poleward Contraction

Similar to Figure 2, Figure 3 shows the change in the latitude of the OCB for onsets at latitudes (a) 66–68°, (b) 64–66°, (c) 62–64° and (d) <62°. For brevity and clarity, only the results from WIC are presented. As the results from SI12 and SI13 are morphologically similar (as per Figure 2), similar figures from SI12 and SI13 are provided in the supporting information. The results from all substorm onset latitude categories show similar behavior to the 64–66° onset latitude category as shown in Figure 2, with an equatorward expansion of the OCB prior to substorm onset which continues away from the onset MLT until ~30 minutes after onset, while the OCB in MLT sectors close to the onset sector rapidly contracted poleward. For the highest latitude onsets, the OCB in the sectors close to the onset sector reached its most equatorward position prior to substorm onset. Furthermore, the OCB does not expand as much prior to onset for these events. A smaller expansion of the OCB prior to substorm onset is consistent with higher onset latitude substorms accumulating less open flux before substorm onset and hence being associated with smaller substorms (Milan, Grocott, et al., 2009). In addition, some of the brightenings in the higher latitude substorm onset categories identified by Frey et al. (2004) may be poleward boundary intensifications (De la Beaujardiére et al., 1994) or pseudobreakups rather than substorms that do not necessarily have an increase in open flux prior to the observed brightening.

In Figures 2 and 3, the time of the most equatorward location of the OCB in each MLT sector is indicated by a black cross or dot. For all onset latitude categories, the OCB reaches its most equatorward latitude within 30 minutes of substorm onset in the majority of MLT sectors with the OCB in MLT sectors further from the substorm onset MLT contracting poleward at increasingly later times. This shows an apparent duskward and dawnward motion or expansion of the region of contracting OCB. Linear regression was used to fit this motion toward dusk and dawn. The data points included in the analysis were varied by including or excluding the three data points from either end, that is, around the substorm onset sector and the far dusk and dawn MLT sectors. The statistical R^2 value indicating the goodness of fit of the line was used to determine the line of best fit. In Figures 2 and 3, the crosses show the data points used to provide the best fit lines given in the figures. The results of the linear regression analysis are presented in Table 1. The slopes presented in Table 1 are from the line of best fit analysis, and the average gradients across all the FUV data sets for each substorm onset latitude category are also shown.

In Table 1, the R^2 values are higher than 0.5 with the exception of the dawnward gradients from WIC and generally higher than 0.7. These high R^2 values indicate that fitting a linear gradient is a reasonable assumption and generally provides a good fit to the data across all substorm onset latitude categories. In the mean gradients averaged across all three IMAGE FUV data sets, the apparent dawnward motion is slightly slower (~|0.2| MLT hours/minutes) than the duskward motion (~|0.3|MLT hours/minutes) corresponding to a speed of approximately 1.1 km/s at 65°. This may be indicative of the westward traveling surge; however, we note that the difference of 0.1 MLT hours/minutes is comparable to the level of uncertainty in our analysis.

Table 1
The Dawnward and Duskward Expansion of Flux Closure

	Dawnward							Duskward						
	SI12		WIC		SI13			SI12		WIC		SI13		
Onset latitude (°)	Gradient (MLT hours/minutes)	R^2	Gradient (MLT hours/minutes)	R^2	Gradient (MLT hours/minutes)	R^2	Mean gradient (MLT hours/minutes)	Gradient (MLT hours/minutes)	R^2	Gradient (MLT hours/minutes)	R^2	Gradient (MLT hours/minutes)	R^2	Mean gradient (MLT hours/minutes)
66–68	0.4	0.56	0.20	0.73	0.00	0.54	0.1	−0.10	0.86	−0.20	0.98	−0.10	0.97	−0.1
64–66	0.1	0.73	0.10	0.94	0.20	0.77	0.1	−0.20	0.88	−0.20	0.97	−0.50	0.69	−0.3
62–64	0.3	0.87	0.40	0.43	0.20	0.84	0.3	−0.20	0.93	−0.20	0.94	−0.10	0.82	−0.2
<62	0.1	0.97	0.20	0.44	0.20	0.89	0.2	−0.70	0.53	−0.20	0.95	−0.70	0.94	−0.5

There are some differences in the gradients derived from the three instrument data sets. In general, the gradients derived from the WIC data are similar in both the dawnward and duskward directions and are consistent across all substorm onset categories. The dawnward gradients derived from the SI12 data and the duskward gradients derived from the SI13 data tend to be more varied, across the substorm onset latitude categories. The largest gradients in the duskward direction tend to be found in the SI13 data, particularly in the lowest onset latitude substorm categories of less than 62°. The largest gradients in the dawnward direction are found in the lower onset latitude categories in the SI12 data (less than 62°) and in the WIC data (62–64°).

3.4. Nightside Flux Content

The open flux content on the nightside is calculated by using the OCB location to determine the approximate area of each MLT sector and then multiplying this by the magnetic field threading through that sector. The summation of the flux from each MLT sector then provides an estimate of the nightside flux content. Here, we calculate the flux from the −6 to +6 MLT sectors for all three FUV instruments. Figure 4 shows the results of a superposed epoch analysis of the total nightside flux content during the hour prior to and after substorm onset for all instrument data, at all onset latitudes.

For substorms at all latitudes, the average nightside flux content increases prior to substorm onset, consistent with the accumulation of open flux content during the substorm growth phase, and decreases immediately after onset, indicating that nightside reconnection becomes dominant over dayside reconnection at substorm onset. This is observed across all FUV imagers. The continued decrease in the total nightside flux content during the hour after substorm onset suggests that the flux content continues to decrease even after the end of substorm expansion phase, typically 20–30 minutes after onset, and into the recovery phase.

While the overall trends in open flux are similar for each imager and all onset latitudes, there are subtle differences in the flux profiles. The nightside flux from WIC is ~0.05 GWb lower than that calculated from SI12 and SI13, which are approximately equal for all but the lowest onset events (Figure 4d). This corresponds to a percentage difference of 7–10% of the nightside open flux content at onset and shows no apparent dependence on onset latitude. The flux profile from WIC for the lowest latitude events shows a plateau in the total nightside flux content for 10 minutes after substorm onset. This result is not replicated in the results of any other substorm onset category or in the SI12 or SI13 data for the same substorm onset latitude category. The SI13 data shows a slightly sharper peak at substorm onset compared to the WIC and SI12 profiles in the low to mid substorm onset latitude categories.

By linearly fitting the rate of change in the total nightside flux content during the 30 minutes before and after substorm onset, we have determined the net difference in the dayside and nightside reconnection rates in terms of a difference in reconnection voltage (Table 2). The change in flux content during both the periods before and after onset is greatest for the lowest latitude events and decreases with onset latitude, in keeping with previous results (e.g., Milan, Grocott, et al., 2009). The rates of change of flux are 1.7–3.4 times greater for the substorms with onsets of less than 62° compared to onsets in the 66–68° range. Similarly, the loss of open flux occurs more quickly than the increase in flux prior to onset. For the highest onset latitude events,

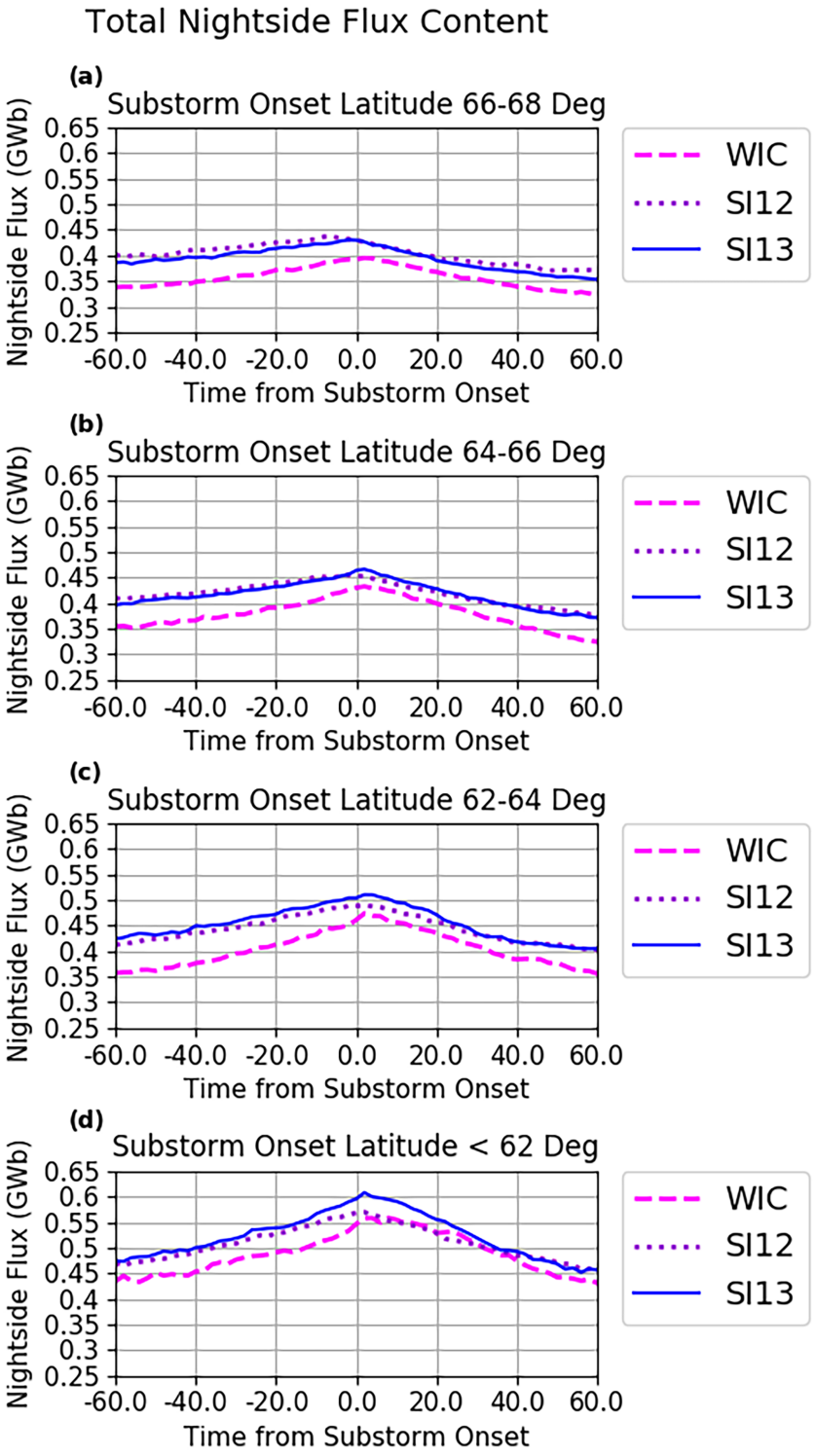

Figure 4. Results of superposed epoch analysis of the total nightside flux content calculated between MLT sectors −6 and MLT +6 for each of the three FUV instruments in the 1 hours before and after substorm onset. WIC data are shown in pink, SI12 data are shown in purple, and SI13 data are shown in blue. (a) shows the total nightside flux content for the highest substorm onset latitude category with the substorm onset latitudes decreasing in (b)–(d).

Table 2
– Estimated Net Difference Between Dayside and Nightside Reconnection Rates

Substorm onset latitude (°)	Growth phase (kV)			Expansion phase (kV)		
	SI12	SI13	WIC	SI12	SI13	WIC
66–68	8.0	12.2	15.1	−16.6	−21.3	−19.3
64–66	12.5	18.8	21.0	−20.4	−25.7	−29.4
62–64	21.4	22.3	29.0	−23.8	−27.6	−29.3
<62	27.3	33.7	31.0	−30.3	−38.8	−32.0

flux is closed 1.3–2.1 times faster than it was opened, whereas for the lowest latitude events, flux is only closed 1.0–1.2 times faster than it was opened.

During both the substorm growth and expansion phases, in all substorm onset latitude categories, the rate of change of flux estimated from the SI12 data is consistently the smallest out of the three FUV data sets. In the growth phase, when the balance between dayside and nightside reconnection is dominated by dayside reconnection, the rate of increase of flux estimated from the WIC data is largest for all substorm onset latitude categories, except the lowest onset latitude category (less than 62°) where the SI13 data show the largest rate of increase in the flux content. In the substorm expansion phase, when nightside reconnection dominates, the WIC data show the largest rate of decrease in the total nightside flux content during the 30 minutes after substorm onset for all substorm onset categories, except less than 62° and 66–68°. During the 30 minutes following substorm onset, the percentage difference in the total nightside flux closure estimated from the three FUV instruments is between 5% and 66%. The largest percentage difference is between the WIC and SI13 instruments for substorms with onset latitudes of less than 62°.

Figure 5 shows the contribution to the total nightside flux content from WIC for five representative MLT sectors during the hour before and after substorm onset. The flux contribution from the substorm onset MLT sector (MLT 0) is shown in solid black, a preonset sector (MLT −3) in solid blue, a dusk sector (MLT −6) in dashed blue, a postonset sector (MLT +3) in solid red, and a dawn sector (MLT +6) in dashed red.

Since the auroral oval is not centered on the magnetic pole, the OCB is generally more equatorward on the nightside than at dusk and dawn. As such, our MLT 0 sector contains the largest contribution to the total nightside flux content, approximately 10% for all substorm onset latitude categories. The preonset and postonset MLT sectors (MLT −3 and MLT +3, respectively) contribute approximately equal amounts of flux to the total nightside flux content throughout the 2 hours period encompassing onset, each containing ~8% of the total nightside flux content at substorm onset. The dawn and dusk MLT sectors (MLT +6 and MLT −6) contain the smallest amount of flux in the nightside MLT sectors, each contributing approximately 5–6% to the total nightside flux content, in all substorm onset latitude categories. At substorm onset, the open flux in the onset MLT sector shows an immediate and abrupt change from increasing flux to decreasing flux for onsets at all latitudes and then continues to gradually decrease throughout the hour after substorm onset. One hour after substorm onset, the flux content of the onset MLT sector is slightly lower compared to the flux content 1 hours prior to substorm onset. The open flux in the preonset and postonset (MLT −3 and MLT +3) sectors changes more gradually, plateauing at substorm onset. The flux content in these sectors is observed to start to decrease within 10–20 minutes of substorm onset in keeping with the continued equatorward expansion of the OCB in Figures 2 and 3. In the dawn and dusk sectors (MLT +6 and MLT −6), there is a much smaller change in the flux content over the 2 hours period; however, the flux content of these MLT sectors is observed to increase prior to substorm onset and continue to increase for up to 10–30 minutes after onset. Approximately 30–40 minutes after substorm onset, a slight decrease in the flux content is observed in these MLT sectors for the lower substorm onset latitudes in Panels c–d. In the highest substorm onset latitudes shown in Panels a and b, the flux content of these MLT sectors remains approximately constant during the 40–60 minutes after substorm onset, with no significant change in flux observed.

For onsets above 62°, the preonset and postonset MLT sectors (MLT −3 and MLT +3) and the dawn and dusk sectors (MLT +6 and MLT−6) contain equal amounts of flux throughout the 2 hours period. In the lowest substorm onset latitude category, the flux content of the preonset and dusk MLT sectors is significantly

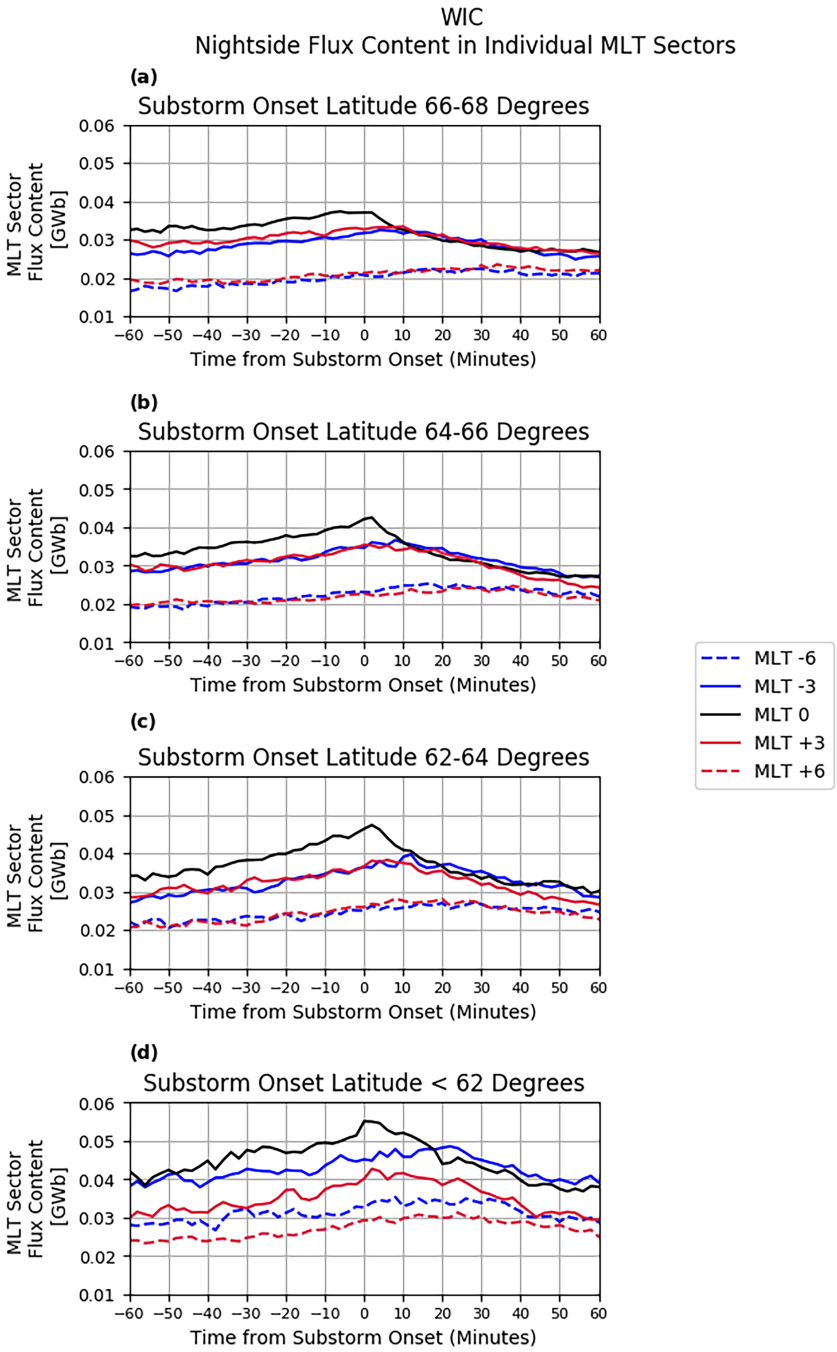

Figure 5. Superposed epoch analysis results of the open flux calculated from WIC from five 1 hours MLT sectors including the substorm onset MLT sector (MLT 0), a preonset MLT sector (MLT −3), a postonset MLT sector (MLT +3), and a dawn (MLT +6) and dusk MLT sector (MLT −6). For clarity, we only show a selection of MLT sectors. The highest substorm onset latitude of 66–68° is shown in (a), with substorm onset latitude decreasing in panels (b)–(d), to the lowest onset latitude category of less than 62° in (d).

higher than the flux content of the corresponding postonset and dawn MLT sectors. In the highest substorm onset latitude category, the opposite is observed in that the flux content of the postonset sectors is marginally higher than that of the preonset MLT sectors. This suggests a dawn/dusk asymmetry in the opening and closure of flux in the highest and lowest substorm onset latitude categories, despite our analysis accounting for dawn/dusk asymmetries by aligning all substorms by substorm onset MLT sector.

As per the above, similar results can be found from the SI12 and SI13 imagers. For completeness, plots of the fluxes in selected MLT sectors from these imagers are provided in the supporting information.

4. Discussion

We have examined the movement of the OCB, based on auroral boundary observations, with respect to substorm onset time and with respect to the substorm onset MLT sector and the effect this has on the calculation of open magnetic flux in the polar cap. A superposed epoch analysis of the OCB latitude showed the OCB does not contract poleward in all local time sectors immediately after substorm onset but continues to expand equatorward for 20–40 minutes after onset at 6 hours of local time away from the onset MLT sector, with the region of contracting OCB expanding dawnward and duskward at 0.2–0.3 MLT/minutes. Despite this continued equatorward expansion in some sectors, the total open flux in the nightside of the polar cap begins to decrease at substorm onset, dominated by the change in OCB location close to the onset MLT sector.

4.1. Suitability of Using the Proxy OCB Determined From Global FUV Auroral Images

In this study, we have used the OCB calculated by Longden et al. (2010) from the PALB derived from global FUV images of the auroral oval from the IMAGE satellite. In each MLT sector, a latitudinal correction is applied to the PALBs derived from Longden et al. (2010). The latitudinal corrections account for the average offset between PALBs derived from auroral FUV images and the location of the OCB inferred from particle precipitation measurements, which provide a more accurate proxy of the OCB location (Boakes et al., 2008; Carbary et al., 2003; Longden et al., 2010). In the noon and midnight sectors, all PALBs were found to lie poleward of the particle precipitation boundary. The advantage of using the PALBs from global auroral image data as an OCB proxy is that the OCB is defined in all MLT sectors around the auroral oval. While particle precipitation measurements from satellites such as DMSP provide the most accurate determination of the OCB location, these measurements are spatially and temporally limited. A superposed epoch analysis of the OCB location during substorms, such as presented in this work, would not be possible without using the corrected PALBs as a proxy for the OCB.

Our results show that there are subtle differences between the OCBs calculated from the WIC, SI12, and SI13 imagers on IMAGE. Overall, the open flux from SI12 and SI13 are similar, while the open flux from WIC is ~10% smaller, despite the corrections applied to the PALBs. This may be the result of the different resolution of the three imagers: For SI12 and SI13, each pixel covered a minimum of 0.94° when looking straight down at the Earth's surface, while each WIC pixel covered a minimum of 0.48°, with this difference in resolution increasing away from the nadir. Note that a 10% difference in flux can be accounted for by approximately a 5% difference in the latitude of the OCB. Comparing the nightside open flux content estimated from each of the three instruments provides an assessment of the uncertainty in the open flux calculation. Alternatively, these results may indicate that the corrections to the PALB have some dependence on geomagnetic activity that is not currently accounted for. It is unclear from the results of our study which of the OCB identifications from each of the three FUV instruments provide the closest boundary identification to the true OCB location or whether the boundaries from any of the instruments consistently over or under estimates the total flux content of the polar cap. The consistently lower estimation of the total nightside flux content from the WIC data is relevant for future upcoming missions, such as SMILE. The SMILE mission will host an UV instrument (UVI) onboard to monitor the northern hemisphere aurora (SMILE Team, 2015). The proposed UVI will have a wide passband sensitive to Lyman-Birge-Hopfield emission which is similar to the passband of the WIC instrument of 140–190 nm. We caution that future estimations of the polar cap flux content using data from the SMILE UVI may slightly underestimate or overestimate the total flux content of the polar cap and, by extension, the net difference in dayside and nightside reconnection rates.

4.2. Expansion of the Contracting OCB Region Toward the Dawn and Dusk Sectors

The formation of an "auroral bulge" and its rapid duskward expansion in a "westward traveling surge" were some of the first reported features of the auroral phenomenology of substorms (Akasofu, 1964), with the westward traveling surge moving at speeds of up to 0.4–2.2 km/s (Craven et al., 1989; Marklund et al., 1998 and Gjerloev et al., 2007). Gjerloev et al. (2007) also found that, on average, the eastward propagation

of the auroral bulge toward the dawn was marginally faster than toward dusk. More recently, using data from the WIC and SI12 instruments on IMAGE, Walach et al. (2017) found that the brightening of the electron auroral oval expanded toward the dawn and dusk sectors 10–40 minutes after substorm onset, during the substorm expansion phase, covering 12 hours of MLT. In contrast, by applying directed network analysis to ground magnetometer data, Orr et al. (2019) found that magnetic perturbations associated with substorm activity and loosely linked to the auroral bulge expanded westward toward the dusk MLT sectors after substorm onset before expanding dawnward at a later time. We found that the average rate of expansion of the region of contracting OCB toward the dawn and dusk directions was |0.2| and |0.3| MLT/minutes, respectively, corresponding to approximately 1.1 km/s at 65° latitude, in agreement with these earlier studies of the expansion of the auroral brightness and westward and eastward moving surges.

Cowley and Lockwood (1992) argued that a localized decrease in the open flux content of the polar cap from nightside reconnection would form a bulge in the OCB that would eventually be redistributed around the polar cap by excited plasma flows. The plasma flows direct the closed flux away from the midnight MLT sector, where nightside reconnection is occurring downtail, toward the dawn and dusk sectors. Our results are in keeping with this ECPC framework, showing that the nightside OCB does not contract poleward uniformly in response to the sudden onset of unbalanced nightside reconnection at substorm onset, but rather, there is a localized contraction which spreads duskward and dawnward. Furthermore, the OCB away from the substorm onset sector continues to move equatorward until the contracting "bulge" expands into those sectors. Overall, in the lower substorm onset latitude categories, the OCB in MLT sectors away from the onset MLT sector continues to expand further toward the equator for longer after substorm onset compared to higher onset latitude substorms. The overall ionospheric convection is enhanced for all substorms to some degree, but there is a localized reduction in the ionospheric return flow in the auroral region close to substorm onset (Provan et al., 2004). Grocott et al. (2009) found that the localized reduction in the flow is more pronounced in low onset latitude substorms (less than 64°) but is less apparent for higher latitude onsets. Combining the results of Grocott et al. (2009) to the continued expansion of the OCB presented here suggests that the reduced ionospheric flows result in a slower redistribution of the flux which is closed as a result of the onset of nightside reconnection at substorm onset, as also suggested by Milan, Hutchinson, et al. (2009). This results in a slower expansion of the poleward contracting region of the OCB during lower onset latitude substorms, particularly in the dawn MLT sector and dusk MLT sectors further from the substorm onset sector.

4.3. Variations in the Total Nightside Flux Content

Using the OCB location to estimate the total nightside flux content calculated over 12 MLT sectors, we have shown that, on average, the total nightside flux content increases before and decreases immediately after substorm onsets identified by Frey et al. (2004) consistent with dayside reconnection being dominant before onset and nightside reconnection being dominant after onset. These results were consistent across each of the IMAGE FUV instruments and across all substorm onset latitude categories. However, the exact timing of substorm onset and hence the ordering of events with respect to onset remain a contentious issue within substorm research. Frey et al. (2004) identified onsets as local brightenings that spread azimuthally in local time for at least 20 minutes. These have an inherent timing uncertainty of ±2 minutes due to observational cadence of the FUV imagers. In addition, small-scale auroral brightenings known as auroral beads (e.g., Kalmoni et al., 2015, 2017) and exponential growth in ultralow frequency wave activity (e.g., Rae et al., 2010), which are reported as the first signatures of substorm activity, can be seen 6–10 minutes before the large-scale auroral enhancements reported by Frey et al. (2004) (Murphy et al., 2009). As such, our results show that, on average, nightside reconnection becomes dominant, and there is a net closure of flux following the large-scale brightening of the aurora; however, other physical processes associated with substorm activity may occur before this.

The total nightside flux content at substorm onset ranged from approximately 0.40 – 0.60 GWb for high to low substorm onset latitudes, respectively. Previous studies have shown the total open flux content at substorm onset to be between 0.53 and 1.01 GWb (Boakes et al., 2011; Coumans et al., 2007; Hubert et al., 2006, 2017); thus, our nightside flux makes up between 60% and 80% of the total flux. This is a natural consequence of the offset of the center of the auroral oval from the magnetic pole, with the

OCB in the midnight sector typically approximately 6–12° further from the pole than in the noon sector (Carbary, 2005; Holzworth & Meng, 1975). Over the hour before onset, the nightside flux increased by 0.05–0.135 GWb or 10–22% of the flux at onset. Boakes et al. (2011) reported that the total flux increased over 5 hours before onset by 22% relative to the flux at the start of the interval. From their figures, we estimate that, over an hour before onset, the total open flux increased by 0.1 GWb or 15% of the flux at onset. Correcting for the fact that our observations are of the nightside only but that the majority of the auroral oval is on the nightside, this implies that the majority of the variation in the location of the OCB during the hour before and after substorm onset is on the nightside.

The rate of change of flux estimated from the three FUV instrument data sets during the growth and expansion phases showed slightly different results. The rate of change of flux estimated from the SI12 data was consistently smaller than the rates estimated from the WIC and SI13 data during both the growth and expansion phases for all substorm onset latitude categories. In general, the rate of change of flux estimated from the WIC data during both the growth and expansion phases were the largest for all substorm onset latitude categories except lowest onset latitude (less than 62°) category where the rates estimated from the SI13 data were largest for both the growth and expansion phases. Although our analysis is based on the Frey et al. (2004) onset list, the data selection criteria mean that the analysis of the WIC, SI12, and SI13 derived OCBs used different numbers of events (Figure 1). We repeated this analysis using only a subset of substorms for which there were successful OCB locations derived from all three FUV instruments but found that this had no impact on the presented results.

Examining the contribution to the total nightside flux content of five individual nightside MLT sectors (onset MLT 0, preonset MLT −3, postonset MLT +3, dawn MLT +6, and dusk MLT −6) showed that the substorm onset MLT sector consistently contained the highest flux content throughout the 2 hours period and decreased sharply at substorm onset, while the postonset and preonset MLT sectors had a more rounded peak in the flux profile. The dawn sector flux profiles were observed to plateau or continue to increase in the hour after substorm onset. We also observed a dawn-dusk asymmetry in the opening and closure of flux during the highest and lowest substorm onset latitude categories. In the lowest substorm onset latitude category (less than 62°), the flux contribution from the duskward MLT sectors was significantly higher than the dawnward MLT sectors, while in the highest latitude substorm onset category (66–68°), the flux contribution from the dawnward sector MLT +3 was marginally larger than the contribution from the duskward sector MLT −3 prior to substorm onset.

The continued equatorward motion of the OCB after substorm has previously been observed in the R1 and R2 currents (Clausen et al., 2012, 2013; Coxon et al., 2014; Milan, Hutchinson, et al., 2009) and also in the continued stretching of the plasma sheet in the dawn and dusk sectors after substorm onset (Ohtani et al., 1991). From these studies, it has been suggested that the total open flux content continues to increase after substorm onset (Clausen et al., 2012, 2013; Coumans et al., 2007; Coxon et al., 2014). Clausen et al. (2012, 2013) and Coxon et al. (2014) use the R1 Birkeland current as a proxy for the OCB location and found that an oval fitted to the boundary of the R1 current (and by proxy, the OCB) continued to expand equatorward for up to 15–20 minutes after substorm onset before contracting poleward. Clausen et al. (2013) showed that the continued expansion in the OCB after substorm onset is particularly notable in the dawn sectors, which is in agreement with the results presented in this study. They suggested that the continued expansion after substorm onset may be due to dayside reconnection initially dominating over nightside reconnection in the dawn and dusk sectors after substorm onset. Coxon et al. (2018) observed a 20 minute plateau in the magnetic energy density of the magnetotail lobes around substorm onset. The authors suggested that this may be due to a 15 minutes uncertainty in the timing of the substorm onset which may also provide an alternative explanation for the delayed poleward contraction of the OCB observed by Coxon et al. (2014). Our results show that the OCB continues to move equatorward after onset in those MLT sectors far from the onset sector and may indicate a movement of open flux propagating toward dawn and dusk sectors before the closure of flux from nightside reconnection propagates round from the substorm onset sector. The contraction of the OCB close to the onset sector is greater than the continued expansion, and thus, there is a net decrease in open flux after substorm onset. The apparent discrepancy between our results, showing a net closure of flux after onset, and the results of Clausen et al. (2012, 2013) and Coxon et al. (2014), showing a

continued increase in open flux after onset, may explained by dayside reconnection continuing to add more flux than is removed by nightside reconnection immediately after substorm onset, as has been suggested by these studies. It may be that it is not until a later time after substorm onset when the closure of flux as a result of nightside reconnection spreads toward dawnward and duskward MLT sectors that the flux closure begins to dominate and the total flux content decreases. In this study, we have only been able to study the change in the flux content of the nightside MLT sectors during substorms and infer the rates of nightside reconnection, but we have been unable to include the changes in the flux content of the dayside MLT sectors or reconnection rates.

An alternative explanation is that as most local times show a slight equatorward motion of the OCB after substorm onset, the oval-fitting method used by Clausen et al. (2012, 2013) and Coxon et al. (2014) fits to this equatorward motion, suggesting a continued increase in the open flux content but the localized contraction of the OCB in the substorm onset sectors is larger than the ongoing expansion, resulting in a net decrease in flux. In both cases, the distorted shape of the OCB is key to understanding the changes in open flux during substorms.

5. Conclusions

During substorms, the OCB in all nightside MLT sectors is observed to expand toward the equator during the growth phase indicative of open magnetic flux accumulating in the polar cap. At substorm onset, the OCB in MLT sectors around the substorm onset sector immediately contracts poleward, while the OCB in MLT sectors in the dawn and dusk regions continues to expand toward the equator. After substorm onset, the poleward contraction of the OCB appears to propagate away from the substorm onset sectors round toward the dawn and dusk regions. This results in the OCB in MLT sectors furthest from the onset sector continuing to expand toward the equator for longer after substorm onset. The apparent motion of the flux closure away from the substorm onset MLT sectors was found to be slightly faster in the duskward direction, indicating that the OCB in the dusk sectors begins to contract poleward slightly earlier while the OCB in the dawn sectors continues to expand equatorward.

After substorm onset and into the expansion phase, the magnetic flux content of the dusk and dawn sectors (MLT −6 and MLT +6) continues to increase, as indicated by the continued equatorward expansion. However, the total nightside flux content decreases immediately at substorm onset. The decrease in the flux content of the onset MLT sector is shown to dominate the overall decrease in the total nightside flux content, despite the continued increase in the flux content observed in the far dusk and dawn sectors.

The total nightside flux content estimated from each of the three FUV instrument data sets differed by up to 10% at substorm onset. The WIC data set consistently estimated the lowest nightside flux content at substorm onset compared to the SI12 and SI13 data sets. The lower nightside flux content estimated from WIC data is relevant for scientific analysis of the polar cap flux content from future missions which will host a wideband UV instrument similar to WIC, such as the upcoming SMILE mission.

Acknowledgments
M. K. M.'s studentship is funded by the U.K. Natural Environment Research Council. C. F. is funded by a NERC Independent Research Fellowship NE/N014480/2. J. C. C. was supported on STFC Consolidated Grant ST/R000719/1. Auroral boundary data were derived and provided by the British Antarctic Survey based on IMAGE satellite data (https://www.bas.ac.uk/project/image-auroral-boundary-data/). The authors would like to thank the NASA Space Physics Data Facility and National Space Science Data Center. The IMAGE FUV data are provided courtesy of the instrument PI Stephen Mende (University of California, Berkeley). We thank the PI, the IMAGE mission, and the IMAGE FUV team for data usage and processing tools.

References

Akasofu, S.-I. (1964). The development of the auroral substorm. *Planetary and Space Science*, *12*, 273–282. https://doi.org/10.1016/0032-0633(64)90151-5

Baker, J. B., Clauer, C. R., Ridley, A. J., Papitashvili, V. O., Brittnacher, M. J., & Newell, P. T. (2000). The nightside poleward boundary of the auroral oval as seen by DMSP and the Ultraviolet Imager. *Journal of Geophysical Research*, *105*. https://doi.org/10.1029/1999JA000363

Boakes, P. D., Milan, S. E., Abel, G. A., Freeman, M. P., Chisham, G., & Hubert, B. (2009). A statistical study of the open magnetic flux content at the time of substorm onset. *Geophysical Research Letters*, *36*, L04105. https://doi.org/10.1029/2008GL037059

Boakes, P. D., Milan, S. E., Abel, G. A., Freeman, M. P., Chisham, G., & Hubert, B. (2011). A superposed epoch investigation of the relation between magnetospheric solar wind driving and substorm dynamics with geosynchronous particle injection signatures. *Journal of Geophysical Research*, *116*, A01214. https://doi.org/10.1029/2010JA016007

Boakes, P. D., Milan, S. E., Abel, G. A., Freeman, M. P., Chisham, G., Hubert, B., & Sotirelis, T. (2008). On the use of IMAGE FUV for estimating the latitude of the open/closed magnetic field line boundary in the ionosphere. *Annales Geophysicae*, *26*, 2759–2769. https://doi.org/10.5194/angeo-26-2759-2008

Burch, J. L. (2000). IMAGE mission overview. *Space Science Reviews*, *91*, 1–14. https://doi.org/10.1023/A:1005245323115

Carbary, J. F. (2005). A Kp-based model of auroral boundaries. *Space Weather*, *3*, S10001. https://doi.org/10.1029/2005SW000162

Carbary, J. F., Sotirelis, T., Newell, P. T., & Meng, C.-I. (2003). Auroral boundary correlations between UVI and DMSP. *Journal of Geophysical Research*, *108*(A1), 1018. https://doi.org/10.1029/2002JA009378

Chisham, G., Freeman, M. P., Abel, G. A., Lam, M. M., Pinnock, M., Coleman, I. J., et al. (2008). Remote sensing of the spatial and temporal structure of magnetopause and magnetotail reconnection from the ionosphere. *Reviews of Geophysics*, *36*, RG1004. https://doi.org/10.1029/2007RG000223

Chu, X., McPherron, R. L., Hsu, T.-S., & Angelopoulos, V. (2015). Solar cycle dependence of substorm occurrence and duration: Implications for onset. *Journal of Geophysical Research: Space Physics*, *120*, 2808–2818. https://doi.org/10.1002/2015JA021104

Clausen, L. B. N., Baker, J. B. H., Ruohoniemi, J. M., Milan, S. E., & Anderson, B. J. (2012). Dynamics of the region 1 Birkeland current oval derived from the Active Magnetosphere and Planetary Electrodynamics Response Experiment (AMPERE). *Journal of Geophysical Research*, *117*, A06233. https://doi.org/10.1029/2012JA017666

Clausen, L. B. N., Baker, J. B. H., Ruohoniemi, J. M., Milan, S. E., Coxon, J. C., Wing, S., et al. (2013). Temporal and spatial dynamics of the regions 1 and 2 Birkeland currents during substorms. *Journal of Geophysical Research: Space Physics*, *118*, 3007–3016. https://doi.org/10.1002/jgra.50288

Coumans, V., Blockx, C., GéRard, J.-C., Hubert, B., & Connors, M. (2007). Global morphology of substorm growth phases observed by the IMAGE-SI12 imager. *Journal of Geophysical Research*, *112*, A11211. https://doi.org/10.1029/2007JA012329

Cowley, S. W. H., & Lockwood, M. (1992). Excitation and decay of solar wind-driven flows in the magnetosphere-ionosphere system. *Annales Geophysicae*, *10*, 103–115.

Coxon, J. C., Freeman, M. P., Jackman, C. M., Forsyth, C., Rae, I. J., & Fear, R. C. (2018). Tailward propagation of magnetic energy density variations with respect to substorm onset times. *Journal of Geophysical Research, Space Physics*: *123*, 4741–4754. https://doi.org/10.1029/2017JA025147

Coxon, J. C., Milan, S. E., Clausen, L. B. N., Anderson, B. J., & Korth, H. (2014). A superposed epoch analysis of the regions 1 and 2 Birkeland currents observed by AMPERE during substorms. *Journal of Geophysical Research: Space Physics*, *119*, 9834–9846. https://doi.org/10.1002/2014JA020500

Coxon, J. C., Rae, I. J., Forsyth, C., Jackman, C. M., Fear, R. C., & Anderson, B. J. (2017). Birkeland currents during substorms: Statistical evidence for intensifications of Region 1 and 2 currents after onset and a localized signature of auroral dimming. *Journal of Geophysical Research: Space Physics*, *122*, 6455–6568. https://doi.org/10.1002/2017JA023967

Craven, J. D., Frank, L. A., & Akasofu, S. -I. (1989). Propagation of a westward traveling surge and the development of persistent auroral features. *Journal of Geophysical Research*, *94*, 6961–6967. https://doi.org/10.1029/JA094iA06p06961

De la Beaujardiére, O., Lyons, L. R., Ruohonieme, J. M., Friis-Christensen, E., Danielsen, C., Rich, F. J., & Newell, P. T. (1994). Quiet-time intensifications along the poleward auroral boundary near midnight. *Journal of Geophysical Research*, *99*(A1), 287–298. https://doi.org/10.1029/93JA01947

Dungey, J. W. (1961). Interplanetary magnetic field and the auroral zones. *Physical Review Letters*, *6*(2), 47–48. https://doi.org/10.1103/physrevlett.6.47

Forsyth, C., Rae, I. J., Coxon, J. C., Freeman, M. P., Jackman, C. M., Gjerloev, J., & Fazakerley, A. (2015). N.:A new technique for determining Substorm Onsets and Phases from Indices of the Electrojet (SOPHIE). *Journal of Geophysical Research: Space Physics*, *120*, 10,592–10,606. https://doi.org/10.1002/2015JA021343

Frey, H. U., & Mende, S. B. (2007). Substorm onsets as observed by IMAGE-FUV. In M. T. Syrjäsuo & E. Donovan (Eds.), *Proceedings of the Eighth International Conference on Substorms (ICS-8)* (pp. 71–75). Alberta, Canada: University of Calgary.

Frey, H. U., Mende, S. B., Angelopoulos, V., & Donovan, E. F. (2004). Substorm onset observations by IMAGE-FUV. *Journal of Geophysical Research*, *109*, A10304. https://doi.org/10.1029/2004JA010607

Gjerloev, J. W., Hoffman, R. A., Sigwarth, J. B., & Frank, L. A. (2007). Statistical description of the bulge-type auroral substorm in the far ultraviolet. *Journal of Geophysical Research*, *112*, A07213. https://doi.org/10.1029/2006JA012189

Grocott, A., Wild, J. A., Milan, S. E., & Yeoman, T. K. (2009). Superposed epoch analysis of the ionospheric convection evolution during substorms: Onset latitude dependence. *Annales Geophysicae*, *27*, 591–600. https://doi.org/10.5194/angeo-27-591-2009

Holzworth, R. H., & Meng, C.-I. (1975). Mathematical representation of the auroral oval. *Geophysical Research Letters*, *2*, 377–380. https://doi.org/10.1029/GL002i009p00377

Hubert, B., Aikio, A. T., Amm, O., Pitkänen, T., Kauristie, K., Milan, S. E., et al. (2010). Comparison of the open-closed field line boundary location inferred using IMAGE-FUV SI12 images and EISCAT radar observations. *Annales Geophysicae*, *28*, 883–892. https://doi.org/10.5194/angeo-28-883-2010

Hubert, B., Gérard, J.-C., Milan, S. E., & Cowley, S. W. H. (2017). Magnetic reconnection during steady magnetospheric convection and other magnetospheric modes. *Annales Geophysicae*, *35*, 505–524. https://doi.org/10.5194/angeo-35-505-2017

Hubert, B., Milan, S. E., Grocott, A., Blockx, C., Cowley, S. W. H., & GéRard, J.-C. (2006). Dayside and nightside reconnection rates inferred from IMAGE FUV and Super Dual Auroral Radar Network Data. *Journal of Geophysical Research*, *111*, A03217. https://doi.org/10.1029/2005JA011140

Kallio, E. I., Pulkkinen, T. I., Kiskinen, H. E. J., Viljanen, A., Slavin, J. A., & Ogilvie, K. (2000). Loading-unloading processes in the nightside ionosphere. *Geophysical Research Letters*,1627–1630. https://doi.org/10.1029/1999GL003694

Kalmoni, N. M. E., Rae, I. J., Murphy, K. R., Forsyth, C., Watt, C. E. J., & Owen, C. J. (2017). Statistical azimuthal structuring of the substorm onset arc: Implications for the onset mechanism. *Geophysical Research Letters*, *44*, 2078–2087. https://doi.org/10.1002/2016GL071826

Kalmoni, N. M. E., Rae, I. J., Watt, C. E. J., Murphy, K. R., Forsyth, C., & Owen, C. J. (2015). Statistical characterization of the growth and spatial scales of the substorm onset arc. *Journal of Geophysical Research: Space Physics*, *120*, 8503–8516. https://doi.org/10.1002/2015JA021470

Kauristie, K., Weygand, J., Pulkkinen, T. I., Murphree, J. S., & Newell, P. T. (1999). Size of the auroral oval: UV ovals and precipitation boundaries compared. *Journal of Geophysical Research*, *104*(A2), 2321–2331. https://doi.org/10.1029/1998JA900046

Longden, N., Chisham, G., Freeman, M. P., Abel, G. A., & Sotirelis, T. (2010). Estimating the location of the open-closed magnetic field line boundary from auroral images. *Annales Geophysicae*, *28*(9), 1659–1678. https://doi.org/10.5194/angeo-28-1659-2010

Marklund, G. T., Karlsson, T., Blomberg, L. G., Lindqvist, P.-A., Fälthammar, C.-G., Johnson, M. L., et al. (1998). Observations of the electric field fine structure associated with the westward traveling surge and large-scale auroral spirals. *Journal of Geophysical Research*, *103*, 4125–4144. https://doi.org/10.1029/97JA00558

McPherron, R. L. (1970). Growth phase of magnetospheric substorms. *Journal of Geophysical Research*, *75*, 5592. https://doi.org/10.1029/JA075i028p05592

Mende, S., Frey, H., Morsony, B., & Immel, T. (2003). Statistical behaviour of proton and electron auroras during substorms. *Journal of Geophysical Research*, *108*(A9), 1339. https://doi.org/10.1029/2002JA009751

Mende, S. B., Heetderks, H., Frey, H. U., Lampton, M., Geller, S. P., Abiad, R., et al. (2000). Far ultraviolet imaging from the IMAGE spacecraft. 2. Wideband FUV imaging. *Space Science Reviews*, *91*, 271–285.

Mende, S. B., Heetderks, H., Frey, H. U., Lampton, M., Geller, S. P., Habraken, S., et al. (2000). Far ultraviolet imaging from the IMAGE spacecraft. 1.System design. *Space Science Reviews*, *91*, 243–270.

Mende, S. B., Heetderks, H., Frey, H. U., Stock, J. M., Lampton, M., Geller, S. P., et al. (2000). and Lauche, H.. Far ultraviolet imaging from the IMAGE spacecraft. 3. Spectral imaging of Lyman-α and OI 135.6 nm. *Space Science Reviews*, *91*, 287–318.

Milan, S. E., Boakes, P. D., & Hubert, B. (2008). Response of the expanding/contracting polar cap to weak and strong solar wind driving: Implications for substorm onset. *Journal of Geophysical Research*, *113*, A09215. https://doi.org/10.1029/2008JA013340

Milan, S. E., Grocott, A., Forsyth, C., Imber, S. M., Boakes, P. D., & Hubert, B. (2009). A superposed epoch analysis of auroral evolution during substorm growth, onset and recovery: Open magnetic flux control of substorm intensity. *Annales Geophysicae*, *27*, 659–668. https://doi.org/10.5194/angeo-27-659-2009

Milan, S. E., Grocott, A., & Hubert, B. (2010). A superposed epoch analysis of auroral evolution during substorms: Local time of onset region. *Journal of Geophysical Research*, *115*, A00I04. https://doi.org/10.1029/2010JA015663

Milan, S. E., Hutchinson, J., Boakes, P. D., & Hubert, B. (2009). Influences on the radius of the auroral oval. *Annales Geophysicae*, *27*, 2913–2924. https://doi.org/10.5194/angeo-27-2913-2009

Milan, S. E., Lester, M., Cowley, S. W. H., Oksavik, K., Brittnacher, M., Greenwald, R. A., et al. (2003). Variations in the polar cap area during two substorm cycles. *Annales Geophysicae*, *21*, 1121–1140. https://doi.org/10.5194/angeo-21-1121-2003

Milan, S. E., Provan, G., & Hubert, B. (2007). Magnetic flux transport in the Dungey Cycle: A survey of dayside and nightside reconnection rates. *Journal of Geophysical Research*, *112*, A01209. https://doi.org/10.1029/2006JA011642

Murphy, K. R., Rae, I. J., Mann, I. R., Walsh, A. P., Milling, D. K., Watt, C. E. J., et al. (2009). Reply to comment by K. Liou and Y.-L Zhang on "Wavelet-based ULF wave diagnosis of substorm expansion phase onset". *Journal of Geophysical Research*, *114*, A10207. https://doi.org/10.1029/2009JA014351

Ohtani, S., Takahashi, K., Zanetti, I. J., Potemra, T. A., McEntire, R. W., & Iijima, T. (1991). Tail current disruption in the geosynchronous region. In J. R. Kan et al. (Eds.), *Magnetospheric Substorms*, *Geophysical Monograph Series* (Vol. 64, pp. 131–137). Washington, DC: American Geophysical Union. https://doi.org/10.1029/GM064p0131

Opgenoorth, H. J., Persson, M. A. L., Pulkkinen, T. I., & Pellinen, R. J. (1994). Recovery phase of magnetospheric substorms and its association with morning-sector aurora. *Journal of Geophysical Research*, *99*, 4115–4129. https://doi.org/10.1029/93JA01502

Orr, L., Chapman, S. C., & Gjerloev, J. W. (2019). Directed network of substorms using SuperMAG ground-based magnetometer data. *Geophysical Research Letters*, *46*, 6268–6278. https://doi.org/10.1029/2019GL082824

Provan, G., Lester, M., Mende, S., & Milan, S. (2004). Statistical study of high-latitude plasma flow during magnetospheric substorms. *Annales Geophysicae*, *22*(10), 3607–3624. https://doi.org/10.5194/angeo-22-3607-2004

Rae, I. J., Kabin, K., Rankin, R., Fenrich, F. R., Liu, W., Wanliss, J. A., et al. (2004). Comparison of photometer and global MHD determination of the open-closed field line boundary. *Journal of Geophysical Research*, *109*, A01204. https://doi.org/10.1029/2003JA009968

Rae, I. J., Watt, C. E. J., Mann, I. R., Murphy, K. R., Samson, J. C., Kabin, K., & Angelopoulos, V. (2010). Optical characterization of the growth and spatial structure of a substorm onset arc. *Journal of Geophysical Research*, *115*. https://doi.org/10.1029/2010JA015376

Siscoe, G. L., & Huang, T. S. (1985). Polar cap inflation and deflation. *Journal of Geophysical Research*, *90*, 543–547. https://doi.org/10.1029/JA090iA01p00543

SMILE Team (2015). SMILE – Payload Definition Document, Rev 2, Issue 3, November 2015, ref ESA_SMILE-EST-PL-DD-001, available at: sci.esa.int/cosmic-vision/57064-request-for-information-rfi-for-the-provision-of-the-payload-module-for-the-joint-esa-china-smile-mission.

Tanskanen, E. (2009). A comprehensive high-throughput analysis of substorms observed by IMAGE magnetometer network: Years 1993–2003 examined. *Journal of Geophysical Research*, *114*, A05204. https://doi.org/10.1029/2008JA013682

Walach, M.-T., Milan, S. E., Murphy, K. R., Carter, J. A., Hubert, B. A., & Grocott, A. (2017). Comparative study of large-scale auroral signatures of substorms, steady magnetospheric convection events, and sawtooth events. *Journal of Geophysical Research: Space Physics*, *122*, 6357–6373. https://doi.org/10.1002/2017JA023991